JGR Atmospheres

RESEARCH ARTICLE
10.1029/2021JD035209

Constraining Aerosol Phase Function Using Dual-View Geostationary Satellites

Qijing Bian[1], Sonia Kreidenweis[1], J. Christine Chiu[1], Steven D. Miller[2], Xiaoguang Xu[3], Jun Wang[4], Ralph A. Kahn[5], James A. Limbacher[5,6], Lorraine A. Remer[3], and Robert C. Levy[5]

[1]Department of Atmospheric Science, Colorado State University, Fort Collins, CO, USA, [2]Cooperative Institute for Research in the Atmosphere, Colorado State University, Fort Collins, CO, USA, [3]Joint Center for Earth Systems Technology, University of Maryland, Baltimore County, MD, USA, [4]Department of Chemical and Biochemical Engineering, University of Iowa, Iowa City, IA, USA, [5]NASA Goddard Space Flight Center, Greenbelt, MD, USA, [6]Science Systems and Applications, Inc., Lanham, MD, USA

Abstract Passive satellite observations play an important role in monitoring global aerosol properties and helping quantify aerosol radiative forcing in the climate system. The quality of aerosol retrievals from the satellite platform relies on well-calibrated radiance measurements from multiple spectral bands, and the availability of appropriate particle optical models. Inaccurate scattering phase function assumptions can introduce large retrieval errors. The high-spatial resolution, dual-view observations from the advanced baseline imagers onboard the two most recent geostationary operational environmental satellites (GOES), East and West, provide a unique opportunity to better constrain the aerosol phase function. Using dual GOES reflectance measurements for a dust event in the Gulf of Mexico in 2019, we demonstrate how a first-guess phase function can be reconstructed by considering the variations in observed scattering angles throughout the day. Using the reconstructed phase function, aerosol optical depth retrievals from the two satellites are self-consistent and agree well with surface-based optical depth estimates. We evaluate our methodology and reconstructed phase function against independent retrievals made from low-Earth-orbit multi-angle observations for a different dust event in 2020. Our new aerosol optical depth retrievals have a root-mean-square-difference of 0.019–0.047. Furthermore, the retrievals between the two geostationary satellites for this case agree within about 0.059 ± 0.072, as compared to larger discrepancies between the operational GOES products at times, which do not employ the dual-view technique.

Key Points:

- Dual, opposing-view geostationary satellite observations help constrain structural properties of dust scattering phase function
- The newly reconstructed phase function produces consistent aerosol optical depth retrievals between the two satellites
- The retrievals between the two satellites agree within 0.059 ± 0.072, compared to 0.157 ± 0.084 in single view retrievals

Correspondence to:
S. Kreidenweis,
soniak@colostate.edu

Citation:
Bian, Q., Kreidenweis, S., Chiu, J. C., Miller, S. D., Xu, X., Wang, J., et al. (2021). Constraining aerosol phase function using dual-view geostationary satellites. *Journal of Geophysical Research: Atmospheres*, *126*, e2021JD035209. https://doi.org/10.1029/2021JD035209

Received 6 MAY 2021
Accepted 24 SEP 2021

1. Introduction

The advent of high-resolution geostationary satellite observations has revolutionized the monitoring of the temporal evolution of myriad atmospheric and surface phenomena. This capability has led to improved weather forecasts (e.g., Mecikalski et al., 2016), insights into cloud microphysical evolution (e.g., Letu et al., 2019), and better tracking of high-impact events that affect human health, such as smoke plumes and blowing dust (Magzamen et al., 2020; Nichols, 2020; Sorensen, et al., 2021). In particular, the two most recent NOAA/NASA Geostationary Operational Environmental Satellites-R series (represented by GOES-East, or GOES-16; and GOES-West, or GOES-17; hereafter, G16 and G17, respectively) provide high quality observations over much of the Western Hemisphere (Figure 1). Among several instruments on board G16 and G17, the advanced baseline imagers (ABI; Schmit et al. [2017]) measure reflectances in the visible, near-infrared, and thermal infrared spectral regions (0.47–13.3 μm) with spatial resolutions of 0.5–2 km, offering ~3× higher spectral, ~4× higher spatial, and ~5× higher temporal resolution compared to the previous-generation GOES imagers.

Over the past several decades, spaceborne multispectral reflectance measurements in the shortwave region have played a key role in characterizing aerosol properties, as demonstrated both in geostationary (Knapp et al., 2005; Zhang et al., 2013) and polar-orbiting platforms (Kahn & Gaitley, 2015; Miller, 2003; Zhou et al., 2020). Most aerosol optical depth (AOD) retrievals are based on single-view, multi-wavelength reflectances. Under cloud-free conditions, the observed reflectance depends on AOD, single scattering albedo (SSA), the scattering phase function, and properties of the underlying surface reflectance. Therefore, the accuracy of aerosol retrieval hinges on how well these components are constrained by either a priori

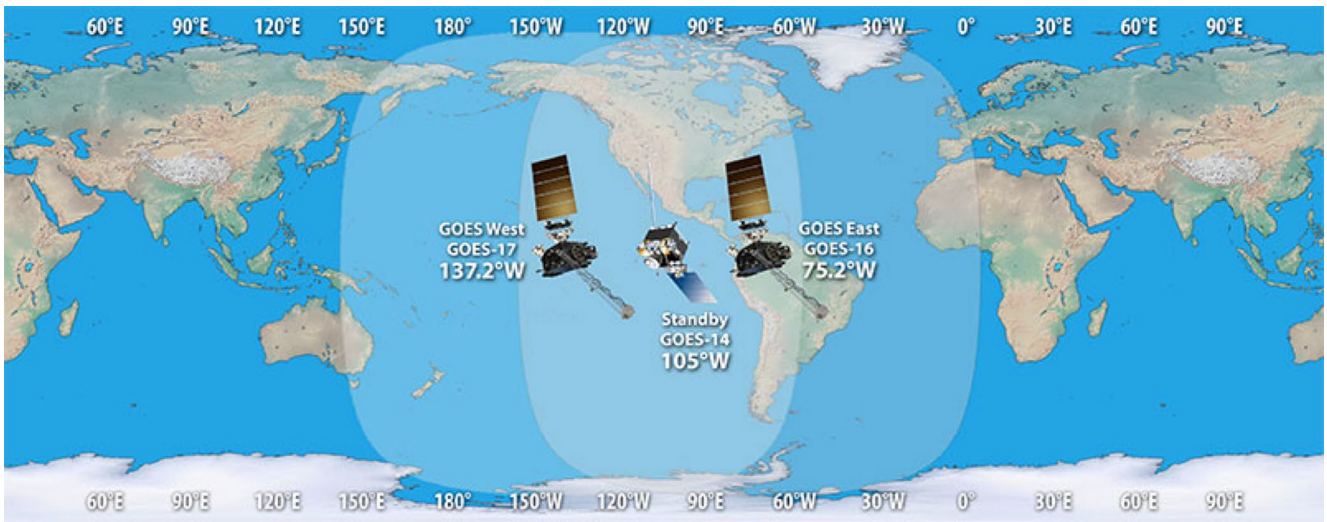

Figure 1. Coverage of GOES-16 and GOES-17. G16 was launched in December 2017 and is located at 75.2° West above the equator; G17 was launched in March 2018 and is located at 137.2° West. This figure is taken from https://www.goes-r.gov/mission/mission.html, credit: NOAA/GOES-R.

information or observations. For example, several studies have demonstrated that incorporating information on aerosol SSA and phase functions from NASA aerosol robotic network (AERONET) observations can greatly improve AOD retrievals (Shi et al., 2019; Yang et al., 2019). Likewise, multi-view measurements such as those from the multi-angle imaging spectroradiometer (MISR) allow better constraints on aerosol model selections (Si et al., 2021) by sampling a portion of the phase function.

As seen in Figure 1, the G16 and G17 ABI fields of view offer considerable overlap over the conterminous United States and the Eastern Pacific Ocean. The dual-viewing geometry available in this broad zone allows for an additional constraint on phase function (Chýlek et al. [2003]; the GOES-R ABI algorithm theoretical basis document (ATBD) (ABI AOD ATBD, 2018)) in ways analogous to MISR retrievals. To understand the potential usefulness of the dual views, Figure 2 highlights the pairs of scattering angles simultaneously observed from G16 and G17 in all seasons for several locations in North America. The corresponding scattering angle combinations largely fall within the range between 90° and 180°, indicating that the dual views would be particularly useful if aerosol phase function features in this scattering range are a focus.

Scattering angles between 90° and 180° are critical for distinguishing between spherical and non-spherical particles (e.g., Kahn et al., 1997). The former are generally consistent with properties of non-absorbing marine and pollution aerosols, whereas the latter are generally consistent with dust particles that have irregular shapes. Although highly scattering spherical particles have a distinct backward scattering peak, non-spherical particles have a relatively smooth phase function structure in the backscattering hemisphere. Despite significant advances in terms of modeling of irregular particles (Saito et al., 2021), *a priori* selection of the most appropriate dust phase function is not straightforward due to the large variability in and a large number of possible combinations of particle size distribution, shape, aspect ratio, and orientation in the atmosphere (Dubovik et al., 2006; Wang et al., 2020).

Because uncertainties in the phase function lead to the largest errors in AOD retrieved at large (i.e., backscatter) scattering angles, Chýlek et al. (2003) suggested circumventing these uncertainties by engineering orbits and viewing geometries such that retrievals are based on moderate scattering angles (50–100°) at which spherical and nonspherical phase function differences are minimal. However, such an orbit design is impractical to achieve large spatial coverage (which often requires a nadir view). In contrast, with GOES-8 data, Wang, Liu, et al. (2003) demonstrated that the backscatter of the same aerosol plume, as viewed from multiple backscattering angles (>110°) over several hours by a geostationary satellite, can provide strong constraints on the aerosol phase function. Here, with more recent and advanced GOES satellites, we propose a new and alternative approach that capitalizes on the differences in *simultaneous* measurements at more than one scattering angle >90° to distinguish between non-absorbing spherical and nonspherical

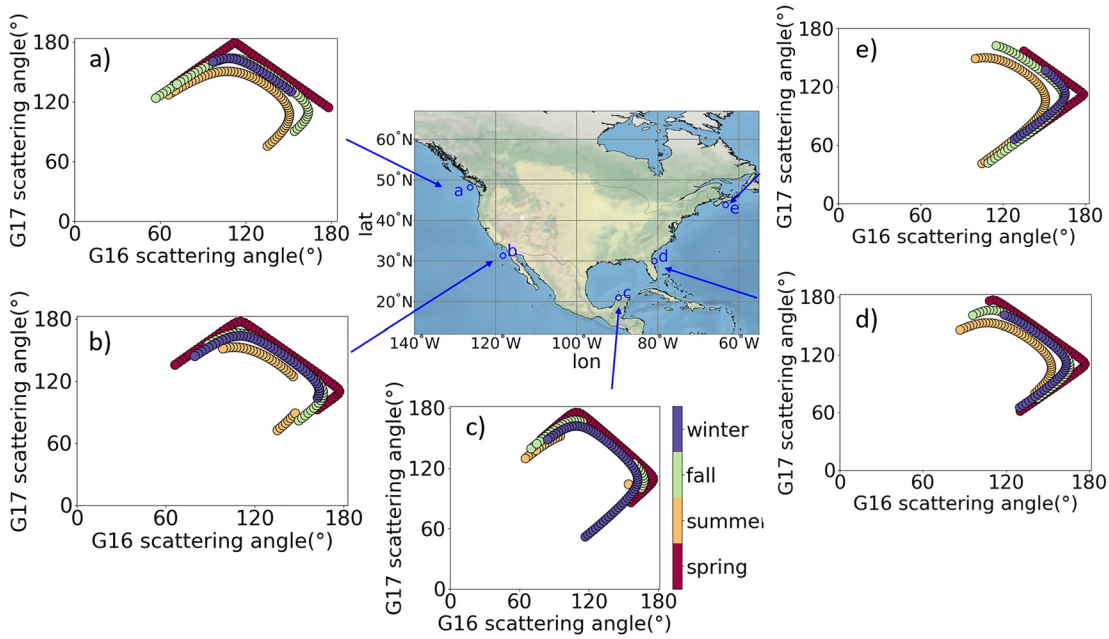

Figure 2. Scattering angle pairs of G16 and G17 for selected locations, including (a) (48°N, 126°W), (b) (31°N 118°W), (c) (21°N, 90°W), that is, the aerosol robotic network Merida site, (d) (30°N, 81°W) and (e) (44°N, 63°W). Calculations were performed over the course of sunrise to sunset on March 1, June 1, September 1, and December 1 to represent different seasons. Defining a sun glint region where the glint angle is less than 40°, color-filled symbols represent that the pixels are outside the sun glint region and can be used in the proposed methodology. Pixels that are within the sun glint region are excluded in this figure and retrievals.

particles. As seen in Figure 2, the G16 and G17 observational pair cover a broad range of scattering angles, most of which are larger than 110°. Therefore, dual-angle retrievals from both G16 and G17 as well as the single-view retrievals from either G16 or G17 will enable large spatial coverage of AOD retrieval while maintaining a simultaneous ability to characterize aerosol phase function.

In this work, we explore a method for leveraging the synergy between G16 and G17 geostationary satellite observations, including the pairs of angles that view the same scene, to determine a best-fit aerosol scattering phase function. Specifically, we propose a method for adjusting an initial guess of a mineral dust phase function to obtain consistent AOD retrievals across the observed scattering angles for a selected case study of a Saharan dust plume that was transported over the Atlantic Ocean and reached the Gulf of Mexico. We test the applicability of the resulting adjusted phase function by retrieving AOD from G16 and G17 reflectances for an additional case of long-range-transported Saharan dust and compare our retrievals with those from the MISR and the operational GOES aerosol products.

2. Methods

2.1. Dust Case Study

The Gulf of Mexico is frequently impacted by long-range transported Saharan dust during the summer season from June to September (Carlson & Prospero, 1972; Prospero & Lamb, 2003). As shown in Figures 1 and 2c, this location resides in the overlap region of G16 and G17, with simultaneous observations available from two view angles. We selected a Saharan dust plume event, which was observed and forecasted (e.g., by the Navy Aerosol Analysis and Prediction System, https://www.nrlmry.navy.mil/aerosol/; Westphal et al. [2009]) in its traverse across the Atlantic Ocean. This plume arrived in the Gulf of Mexico around June 23, 2019. We restricted our study of this case to an over-ocean region to minimize uncertainties associated with land surface reflectance (e.g., Zhang et al., 2020). During this period, fires were observed on the Yucatán peninsula and elsewhere in the region, so that some smoke was likely present in addition to sea salt and dust aerosols. However, the case is dust-dominated, as evidenced by the information to follow.

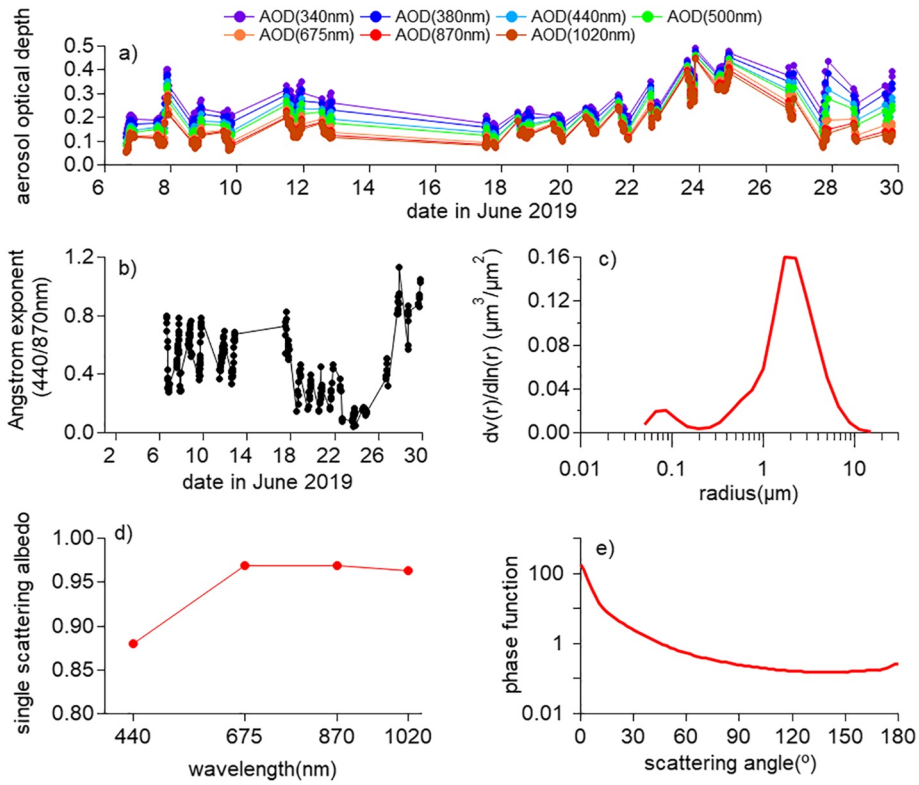

Figure 3. Aerosol Robotic Network (AERONET) Level l.5 retrieval products at the Merida site (Level 2 data were unavailable for this case), used for reconstructing the dust phase function. (a) Aerosol optical depth and (b) extinction Ångström exponent during June 2019. (c), (d) and (e) provide the averaged volume particle size distribution, single scattering albedo, and phase function (at 675 nm), respectively, for June 24, 2019. The AERONET observations are described further in Appendix A.

Data from this Saharan dust-dominated case study are shown in Figure 3. This dust event was clearly seen in the AERONET observations at the Merida site (20.984°N, 89.645°W) on the Yucatán Peninsula, as indicated by the peak in AOD and the weak spectral dependence of AOD (a characteristic of large particles relative to the wavelength of light) (Figure 3a). The only day during the elevated AOD period with reported AERONET particle property retrievals was 24 June. The presence of dust on 24 June was indicated by the small value of the Ångström parameter (Figure 3b) and the retrieved volume size distribution of particles in Figure 3c, which was dominated by the coarse mode. The wavelength dependence of the retrieved single scattering albedo (SSA; Figure 3d) was also similar to that described by Li et al. (2015) for dust. As expected, the retrieved phase functions were flat in the scattering angle range between 100 and 160° (Figure 3e), distinguishing these aerosols from spherical particles.

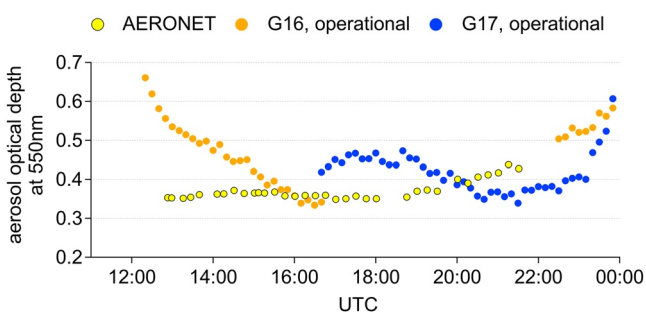

Figure 4. Aerosol Robotic Network -derived aerosol optical depths at 550 nm on June 24, 2019 at the Merida site (20.984°N, 89.645°W), along with G16 and G17 operational products for a pixel located at (21.452°N, 89.604°W). The geostationary operational environmental satellites operational products are described further in Appendix B.

As shown in Figure 4, the AERONET AOD at Merida was fairly constant throughout the day on June 24, 2019. For comparison, G16 and G17 operational (i.e., single-view, stand-alone) AOD retrievals for a coincident oceanic pixel in the Gulf of Mexico near Merida (within ~50 km) are also shown. Their agreement with AERONET is reasonable for part of the day. However, during the periods of temporal overlap, the G16 and G17 AODs are not in agreement with each other, indicative of errors in the surface model, aerosol model, or both. We note that for the latitude, longitude, and date of this case study (Figure 2c), the periods of overlap when both sensors were outside of sun glint were minimal: there was one overlapping time stamp at 16:40 UTC, and a series of nine overlapping points

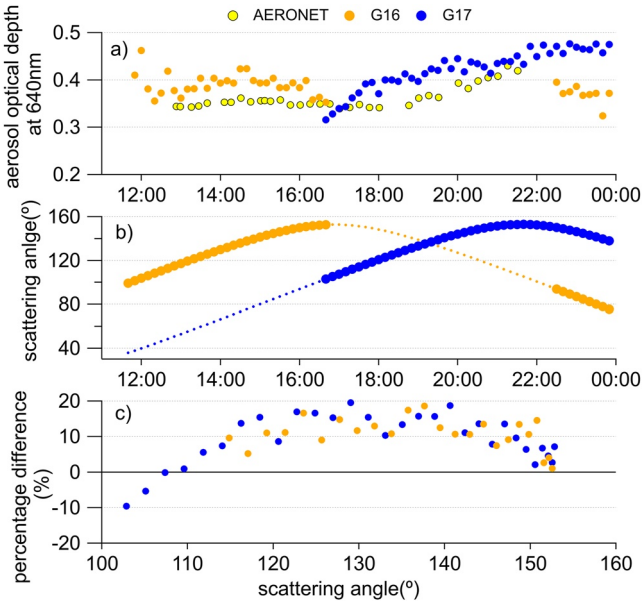

Figure 5. (a) Aerosol optical depth (AOD) retrievals at 640 nm from the AERONET Merida site, and from G16 and G17 observations using the SSA and phase function from the June 24, 2019 Aerosol Robotic Network (AERONET) inversions at Merida. (b) The corresponding scattering angles for G16 and G17 over the course of the case study day. The dotted lines represent data points for which the glint angle is <40°. (c) AOD percentage difference (((retrieved AOD–obs. AOD)/obs. AOD) × 100%) as a function of the scattering angle, where obs. AOD is from AERONET. AERONET AODs were interpolated to the G16 and G17 time stamps for this comparison.

after about 22:00 UTC. Thus, we used comparisons against AERONET and head-to-head comparisons in the post-22:00 UTC time frame when validating this new retrieval scheme.

2.2. Retrieval Method

In GOES Mode 6 operations, the ABI provides full disk images every 10 min and measures radiance in 16 spectral bands. In this study, we used full disk imagery reflectances at the 640 nm wavelength (ABI Band 02; 500 m resolution at nadir) and retrieved AOD over ocean pixels. To retrieve AOD from ABI reflectances, we used a look-up table (LUT) approach, based on calculations from the Unified Linearized Vector Radiative Transfer Model (UNL-VRTM, Xu & Wang, 2019) with VLIDORT (Spurr, 2006) as the core radiative transfer code. The UNL-VRTM has the capability for line-by-line gas absorption calculations from the HITRAN 2012 database (Rothman et al., 2013), including its ancillary UV-visible cross-sections for water vapor continuum absorption and Chappuis ozone absorption (Wang et al., 2014). The model has been validated in and used by several remote sensing theory studies (Ding et al., 2016; Xu & Wang, 2015) and aerosol retrieval algorithms for surface (Xu et al., 2015), airborne (Hou et al., 2020), and space-borne instruments (Xu & Wang, 2019; Xu et al., 2017).

The UNL-VRTM requires aerosol SSA, phase function, optical depth, layer height, and geometric thickness, and ocean surface reflectance to simulate ABI reflectances. The aerosol was represented using the June 24, 2019 AERONET-derived optical properties as a first guess: SSA was therefore set equal to 0.968 (per Figure 3d) and the averaged phase function is shown in Figure 3e was input as discrete points with the same scattering angle resolution as the AERONET product. The LUT was constructed for a uniform aerosol layer at 2–4 km with optical depths varying from 0 to 3. Note that at 640 nm wavelength, the AOD retrieval is not sensitive to the vertical distribution of aerosols (Wang, Christopher, et al., 2003); our test shows that lifting the aerosol layer from 2–4 km to 4–6 km changes AOD less than 2%. The bi-directional ocean reflectance was calculated using the method of Cox and Munk (1954), requiring information on ocean surface wind speed. We input the time-varying wind speed available in the NCEP North American Regional Reanalysis data, which was 7–11 m s^{-1} for this case. To account for water-leaving radiance, a Lambertian albedo of 0.0009–0.0035, calculated offline from the subroutine in the spherical harmonics discrete ordinate method package (SHDOM; Evans [1998]), was added to the final ocean reflectance distribution.

Under these first-guess assumptions, Figure 5a shows the retrieved AOD from G16 and G17 reflectance observations at 640 nm with an on-ground spatial resolution of 500 m. For comparison, AERONET AOD values are also shown, using the Ångström exponent to interpolate to 640 nm. Although the time-dependence of retrieved AOD is more similar to that of AERONET as compared with the GOES operational products shown in Figure 4, both G16 and G17 retrieved AODs are systematically biased high compared to AERONET. Further, as is seen with the GOES operational products, the AODs do not match in the overlap regions, with 4%–20% differences. In this 12-h period, Figure 5b shows that most of the observations occurred for scattering angles >105°, the backscatter region noted by Chýlek et al. (2003) to be most sensitive to uncertainties in the assumed aerosol model. Following Chýlek et al. (2003), we assume that errors in the phase function are more significant than surface reflectance, and seek to improve the retrievals by adjusting the phase function, with a particular focus on the angles at which the mismatch is greatest. This assumption is reasonable based on the sensitivity tests shown in Appendix C, and as discussed further below. As shown in Figure 5c, the differences between the retrieved AODs and the AERONET observations are large for scattering angles between ~110° and 150°, suggesting that changes to the phase function are needed over this range. The methodology for doing so is described in the next section.

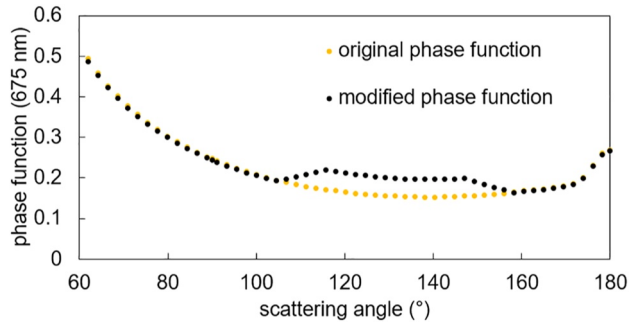

Figure 6. Comparison of original Aerosol Robotic Network phase function (golden dots) and modified phase function (black dots) after increasing the original phase function by 30%. This adjustment was based on the differences between observed and retrieved aerosol optical depths at scattering angles of 110°–150°. The adjusted phase function is smoothed and normalized.

2.3. Adjusting the Phase Function

The ABI-observed reflectance is proportional to the product of ambient AOD, SSA, and phase function. Therefore, to reduce the differences shown in Figure 5c, we tested the impact on the retrievals of phase functions that had been adjusted between scattering angles of ~110°–150° by 20%, 30%, and 35%, respectively. The modified phase functions were smoothed using a moving average with five neighboring values before they were input to the radiative transfer model. SSA was held constant at the original value (0.968) for these tests.

Our results show that the phase function adjusted by 30% (Figure 6) resulted in AOD retrievals that best fit the AERONET observations (±10%, Figure 7). Further, the average percentage difference between G16 and G17 during the overlapping period after 22:00 UTC was reduced to 4% and all differences were within 0.05, which can be explained by the calibration uncertainty in G16 and G17 (see Appendix C). As equivalency of G16 and G17 retrieved AODs during periods of overlap is a requirement for a valid retrieval, this improved agreement further supports that the adjusted phase function is more appropriate to the selected case study.

A few points need to be highlighted here. First, compared to the initial Aerosol Robotic Network phase function, the adjusted phase function has somewhat enhanced side scattering. This enhancement should not be interpreted as a special feature in the dust model, since dual-views from G16 and G17, in this case, do not provide observations for the entire range of scattering angle from 0°−180°. Extending this adjustment approach to various locations and transport events that cover a larger range of angles would help reduce uncertainty in the dust phase function.

Second, in the adjustments above, we have used the AERONET phase function as the first guess, which was retrieved using almucantar scans in 360° azimuth from −5° to 180° and then +5° to −180°. On June 24, 2019, AERONET almucantar data showed that there were five almucantar scans taken, and of those, four reported full inversions. Among these four scans, the largest scattering angles for three of them were 107° or smaller, and the other one was 119°. Therefore, the AERONET phase function has not been well constrained for scattering angles between ~110°−150°, consistent with the range in which the adjustments above are most needed.

Third, to understand the sensitivity of the adjusted phase function to the choice of the first guess, we repeated our methodology, but used the phase function of wet sea salt used in the MODIS and GOES operational retrieval algorithms as the first guess. To make a fair comparison, we used the same SSA = 0.968 in this test. As shown in Figure 8a, the resulting adjusted phase functions are similar regardless of the initial guesses. Even with much larger biases in the initial AOD retrievals as shown in Figure 8b, the adjusted phase function can achieve AODs within 10% of AERONET. However, the same 10% AOD agreement required five more iterations of adjustments if the sea salt phase function was used as the first guess. This is not surprising, because a good first guess helps the solution converge faster, and vice versa if a relatively poor first guess is used. Thus, a better initial guess from AERONET is ideal, but our method is not overly reliant on AERONET inversions in the final adjusted phase function.

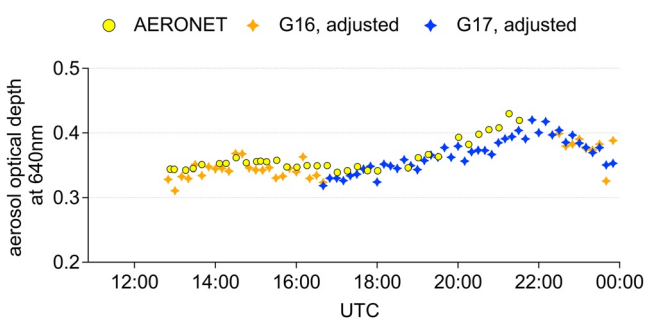

Figure 7. Same as Figure 5a, but using the adjusted phase function shown in Figure 6 to re-build the look-up tables for the G16 and G17 retrievals.

3. Comparisons to Other Independent Retrievals

To test whether the adjusted phase function is applicable to other dust cases observed by G16 and G17, we selected an additional case study from June 2020. The period of interest occurred during a large and extended (mid through late June) Saharan dust transport event that affected the Gulf of Mexico and a large portion of the southeastern United States

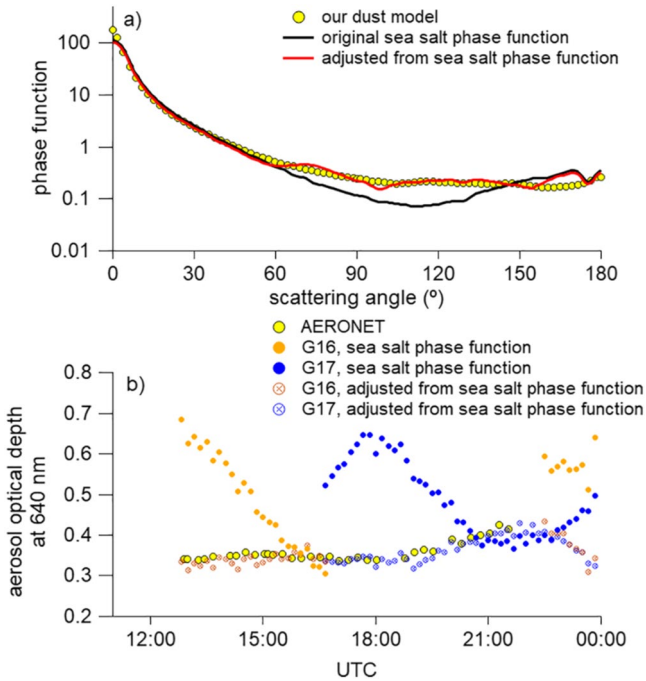

Figure 8. (a) The prior sea salt phase function and the resulting adjusted phase function, both assuming a single scattering albedo of 0.968. For comparison, our adjusted phase function using the Aerosol Robotic Network (AERONET) phase function as the first guess is also shown. (b) aerosol optical depth (AOD) retrievals at 640 nm from G16 and G17 observations using the prior sea salt phase function and the resulting adjusted phase function. AERONET AOD observations (as shown in Figures 5a and 7) are also shown.

(Francis et al., 2020). We conducted retrievals using our methodology and compared them against AODs retrieved from the MISR standard and research algorithms. An ideal case would be associated with the highest AODs observed in the Gulf of Mexico within the main dust plume during June 23–27, 2020. Unfortunately, after excluding cloudy and glint regions and attempting to maximize the overlap time between G16 and G17 retrievals over the MISR swaths, the best case was on June 29, 2020, past the date of the major plume event.

For June 29, 2020, retrievals from the MISR research algorithm (Limbacher & Kahn, 2019) in Figure 9, performed at 1.1 km pixel resolution, shows that the dominant aerosol type over the ocean north and northwest of the Yucatán peninsula was indeed dust-like, with AODs between ~0.4–0.6 (Figure 9a). The mid-visible AOD fraction of non-spherical dust particles was about 0.6 and the fine mode fraction was generally less than 0.4. The single scattering albedo was also consistent with the value found for the June 2019 case study (Figure 3d). These results confirm the dominance of dust aerosol even though the major plume had already passed. Note that the region just north of the Yucatán peninsula was affected by considerable thin cirrus and is very close to the solar equator. Both these conditions affect the quality of the MISR retrievals. In particular, the range of scattering angles observed by MISR is diminished when the sun is high in the sky, which directly affects particle-type discrimination. Therefore, the MISR Research Algorithm used a limited particle climatology to reduce retrieval noise, comprising six-component optical models: three spherical models in common with the MISR standard algorithm, two additional spherical models, and a non-spherical dust optical analog.

Figure 10 shows detailed retrievals for selected pixels that were considered cloud-free and away from glint regions. Our retrievals are based on the adjusted phase function that used the AERONET phase function as the initial guess. All points represent the mean AODs aggregated from pixels within 1.2 km radius regions, and the error bars represent the standard deviation of the retrieval results. In general, the AOD from the MISR Research Algorithm was systematically ~0.015–0.02 higher than the standard algorithm, well within the uncertainty range of the retrievals, and likely attributable to differences in the dust optical model used.

Examining Figure 10, compared to retrievals from the MISR Research Algorithm the operational G16 retrieved AODs were smaller by 0.061 ± 0.032 and the operational G17 AODs were larger by 0.158 ± 0.022. Errors reported here represent the mean absolute bias ±standard deviation. In addition, the differences between G16 and G17 in the operational retrievals were large, indicating errors in the selected aerosol model. Among G16 and G17 retrievals, the retrieval from G17 observations using our adjusted phase function shows the best agreement with MISR, with errors of 0.014 ± 0.012 and a root-mean-square-difference (RMSD) of 0.019; most points fall within one standard deviation of the aggregated MISR retrievals. Our new G16 retrievals are the second closest ones, with errors of 0.040 ± 0.023 and RMSD of 0.047. The G16 and G17 retrievals using our adjusted phase function agreed only within 0.051 ± 0.017 for these selected pixels at this time stamp. Based on the sensitivities shown in Appendix C, this offset can be attributed to calibration differences between the two instruments and errors in modeling ocean surface reflectance.

Although MISR retrievals have the advantage of multi-angle views that are helpful for evaluating the angular dependencies in the GOES retrievals, the MISR overpass time poses challenges. At 16:50 UTC, the corresponding angles over the Gulf of Mexico for G16 and G17 are 152° and 107°, respectively. Recall from Figure 6 that these angles are close to the boundaries of the adjusted portion of the phase function. Therefore, we extended G16 and G17 retrievals to the entire daytime period, evaluating the success of these retrievals by the consistency between G16 and G17 retrievals during periods of overlap.

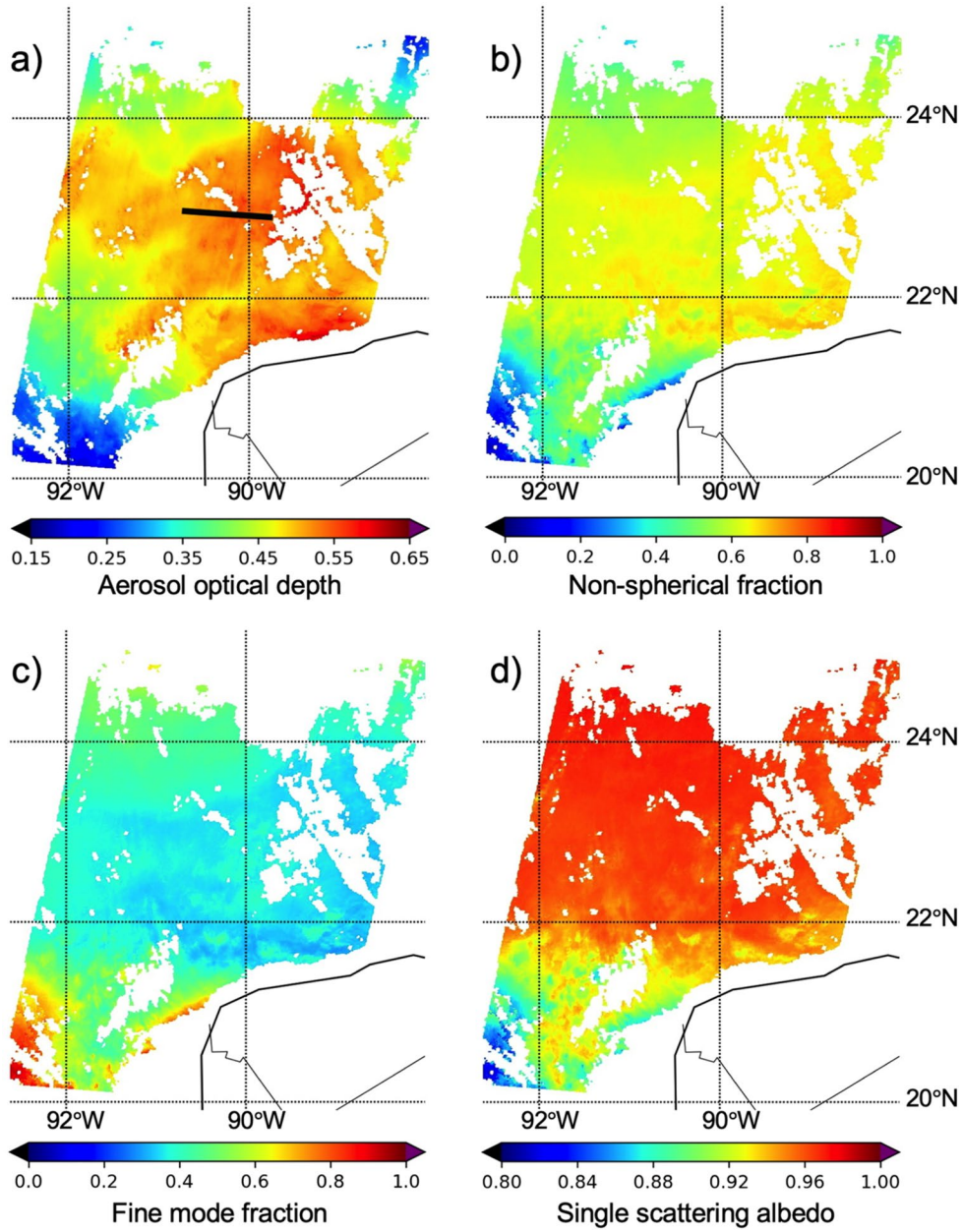

Figure 9. Map of retrieved (a) aerosol optical depth, (b) non-spherical aerosol optical depth (AOD) fraction, (c) fine mode fraction, and (d) single scattering albedo at 16:45 UTC on June 29, 2020, as determined by multi-angle imaging spectroradiometer (MISR) Research Algorithm retrievals for Orbit 109209. Cloud contamination precludes retrievals (white areas) over most of the land (southeast corner) as well as the northern and much of the eastern parts of the scene. In the southwest corner, retrieved particles are smaller, darker, and mostly spherical, likely smoke from the Yucatan. The line in (a) indicates the pixels selected for further intercomparisons. The MISR retrieval products are described further in Appendix B.

Taking retrievals from the 6th and 12th pixel from Figure 10 as examples, Figure 11 shows that the operational G16 and G17 retrievals have very similar patterns–starting with a larger AOD at a scattering angle of ~107° and then decreasing and ending with a smaller AOD at a scattering angle of ~150°. This is a signature of the influence of spherical phase functions, which is not surprising because the operational GOES algorithm employs only spherical aerosol models. The AOD differences between G16 and G17 operational retrievals in all overlap periods for all 20 pixel locations have a mean of 0.157 and a standard deviation of 0.084. In contrast, as shown in Figures 11, G16 and G17 retrievals using the adjusted phase function agreed

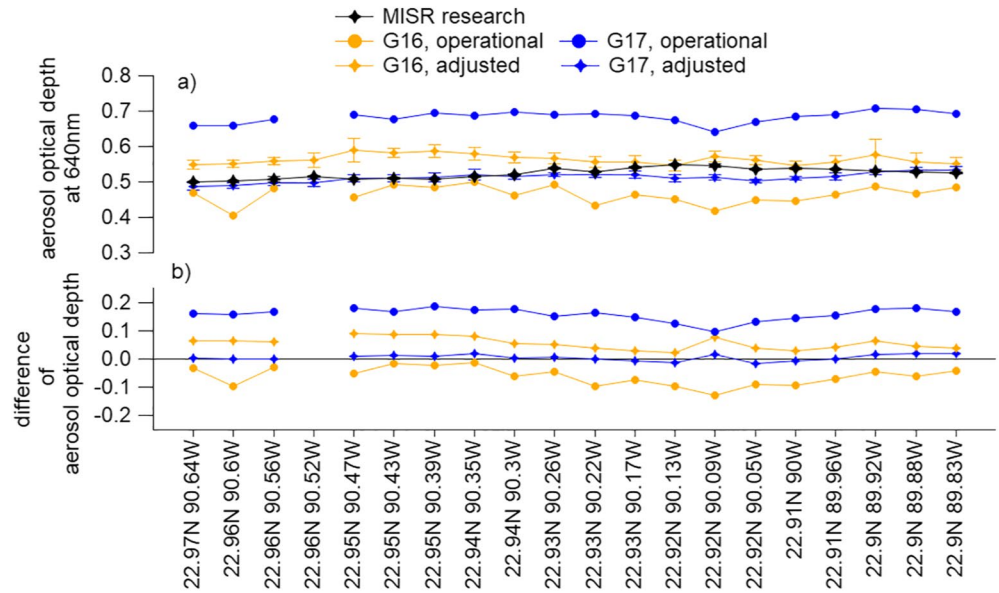

Figure 10. Retrieved aerosol optical depths (AODs) at 640 nm for selected pixels that are marked by a line in Figure 9a. Retrievals include those from the Multi-angle Imaging SpectroRadiometer (MISR) Research Algorithm, the geostationary operational environmental satellites (GOES) operational products, and GOES using our adjusted dust phase function. All products except the ones using the adjusted phase function report AODs at 550 nm and have been converted to 640 nm using spectral scaling coefficients available in the standard MISR product. (b) AOD difference compared to those from the MISR Research Algorithm.

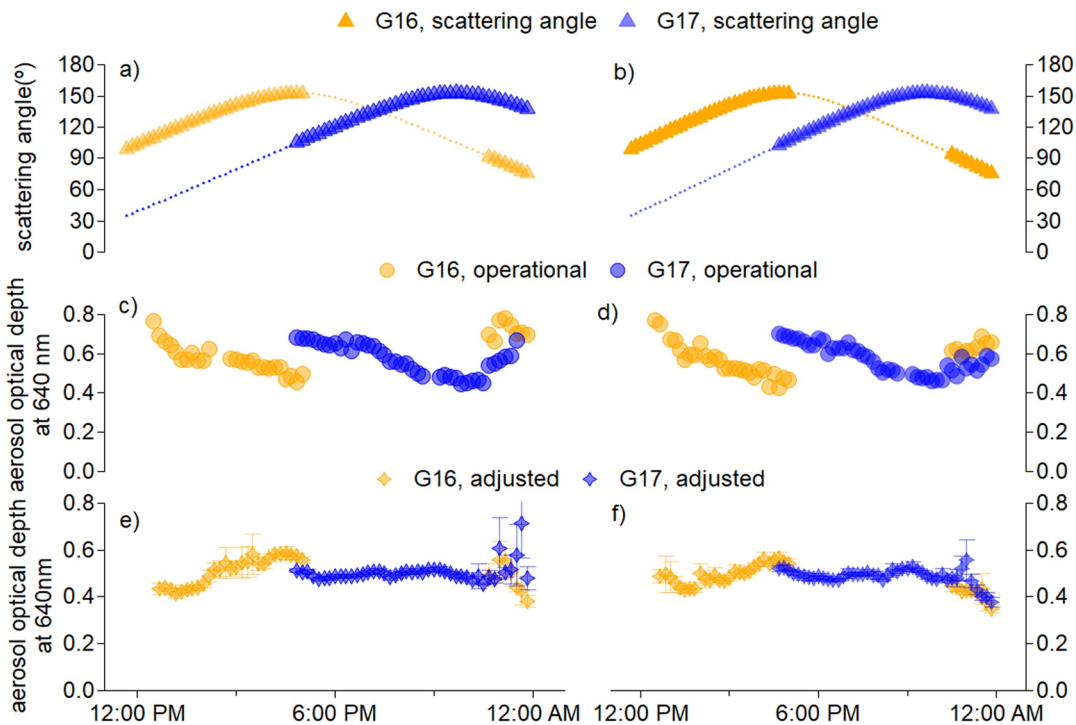

Figure 11. Scattering angle (a) and retrieved aerosol optical depths at 640 nm (c) from the operational geostationary operational environmental satellites products and (e) those using the adjusted phase function for the sixth pixel shown in Figure 10. (b, d, and f) on the right panel are the same as (a, c, and e), respectively, but for the 12th pixel.

well in the overlap periods, with AOD differences of 0.059 ± 0.072 for all 20 pixel-locations (See Appendix D for further details). The improved agreement between the two AODs suggests that the adjusted phase function is more appropriate.

4. Summary

In this study, we explored the use of overlapping ABI observations from GOES-16 and GOES-17 to constrain aerosol retrievals, as well as exploiting observations at specific scattering angles to adjust the shape of an *a priori* phase function used to create look-up tables. The complex nature of mineral dust particles confounds attempts to determine the most appropriate phase functions from the first principles. This difficulty motivated our attempt to use observations directly to deduce a best-fit dust phase function, taking advantage of the ranges of scattering angles represented in the data from the two satellites.

We found that the revised phase function based on the dual-view technique led to better agreement between the G16 and G17 retrievals, compared with the operational products, supporting the validity of the results. Co-locating with AERONET or another measure of AOD was important, as the methodology requires separate, accurate measurements of the AOD to serve as one of the constraints.

The representation of the angular scattering from the surface is also an important consideration in applying this methodology, as it relies so critically on using the variability across scattering angles to evaluate the applied phase function. Over land, as discussed by Zhang et al. (2020), limitations in the representations of land surface reflectances lead to biases in retrievals for geostationary observations. The surface models used in retrievals for polar-orbiting satellite observations have not been optimized for the different geometries accessed by the geostationary instruments. Over-land retrievals present a more challenging situation for our proposed methodology, as both the surface reflectances and the aerosol model may require adjustment. The use of overlapping G16 and G17 observations provides an additional, helpful constraint for such cases.

To improve characterization of the surface, and thereby improve aerosol retrievals, methods have been proposed and applied that is based on combining data from multiple angles that are accessed through multiple overpasses over a time period (e.g., the multiangle implementation of atmospheric correction [MAIAC] algorithm; Lyapustin et al. [2018]). This approach could be leveraged in applying elements of the methodology we have demonstrated to future multi-view retrievals.

In principle, our method can be applied to other dual-view observations, for example, from the series of along track scanning radiometers (ATSR-2 on ERS-2; AATSR on Envisat). Operational algorithms (Bevan et al., 2012; Kolmonen et al., 2013; Sayer et al., 2012; Thomas et al., 2009; Veefkind et al., 1998) have leveraged these multi-angle observations in separating the atmospheric and surface contributions to the top-of-atmosphere reflectances over land. By applying the methodology proposed here, observations of dust plumes over the ocean could be used to assess the predefined dust models used in the current operational algorithms. Another potential application is to observations in the overlapping coverage of G16 and the spinning enhanced visible and infrared imager on the geostationary Meteosat platform. This combination provides an interesting different set of dual-view geostationary observations that can be used in our methodology to investigate the properties of African dust, both closer to its source and as it is transported westward.

Further exploration of our approach can be undertaken by conducting retrievals over AERONET sites that encompass the range of paired observations shown in Figure 2, also covering a range of aerosol types across the varied locations. The approach may be especially useful for smoke, for which differences in optical properties have been shown between fresh and aged emissions, and the findings used to recommend optimized fresh and aged smoke phase functions.

Appendix A: Ground-Based Observations

AERONET is a ground-based worldwide network that has routinely monitored aerosol microphysical and optical properties for more than 25 years (Holben et al., 1998). AERONET is composed of sun/sky radiometers that measure radiance in the visible and near-infrared spectral regions with a 1.2° field-of-view. Direct Sun measurements are used to retrieve aerosol optical depth, whereas sky radiance measurements are used

to retrieve the index of refraction, aerosol size distribution, phase function, and single scattering albedo. As Level 2 products were not available for the sites of interest in this study, we used V3 Level 1.5 products, which are quality controlled through automatic cloud screens but have not had post-field calibrations applied to the retrievals. Although the exact bias and uncertainty in Level 1.5 data are instrument dependent, the differences in AOD between these two levels have a mean of 0.02 and one standard deviations of 0.02 (Giles et al., 2019).

The dust model used in the AERONET retrieval method is detailed in Dubovik et al. (2006). To account for the nonsphericity of dust, they consider mixtures of randomly oriented spheroids with various shapes from flattened to elongated spheroids. By incorporating these mixtures, the resulting phase function was in better agreement with laboratory observations and smoother at scattering angles between 100° and 160° than prior estimates that considered a single fixed axis ratio distribution.

Appendix B: Satellite Data Sets for Evaluation

For pixels over the ocean, the GOES operational aerosol retrieval algorithm (the GOES-R ABI Algorithm Theoretical Basis Document (ABI AOD ATBD, 2018),) used four fine modes and five coarse modes, the same as used in MODIS Collection 5 products (Levy et al., 2007; Remer et al., 2005, 2006). Aerosol retrievals were performed by matching the observed reflectance at 640, 864, 1,610, and 2,240 nm wavelengths with the pre-calculated lookup tables, based on the methods described in Tanré et al. (1997) and Vermote et al. (2006). The AOD retrieval is available at a temporal resolution of 10 min and a spatial resolution of 2 km at nadir. The uncertainty in retrieved AOD over the ocean is reported as 0.03 ± 0.05AOD.

In addition to the operational ABI aerosol product, we compared our retrievals to those from MISR. MISR on the NASA Terra satellite measures reflectances from nine different angles, in each of four spectral bands across the visible and near-infrared (Diner et al., 1998). MISR has a ∼380 km swath and a pixel resolution ranging from 275 m near-nadir to 1.1 km off-nadir. The MISR research algorithm is constructed to optimize particle-type discrimination with 1.1 km pixel-level retrievals and is run on a case-by-case basis (Limbacher & Kahn, 2019). The algorithm includes options to self-consistently retrieve the surface and aerosol or to prescribe the surface from external sources. Retrievals are performed at 1.1 km pixel resolution. Where retrieval conditions are ideal, the algorithm minimizes the cost function using 17 component optical models in the algorithm lookup table. For the dust case analyzed in the current study, the scene was largely cirrus-contaminated and the range of scattering angles was small due to high sun elevation angle, a more limited set of component optical models was used for the retrievals shown in Figures 9 and 10.

Appendix C: Sensitivity Tests

We have conducted sensitivity tests to investigate the impacts of uncertainty in ABI calibration, single scattering albedo, and ocean surface reflectance on AOD retrievals and the adjustments in phase function.

Appendix C1: ABI Calibration Uncertainty

The two ABI sensors on G16 and G17 have been compared with the Visible Infrared Imaging Radiometer Suite (VIIRS) onboard the Suomi National Polar-Orbiting Partnership. G16 and G17 both agree within 5% with VIIRS (Yu et al., 2019). Based on this result, we perturbed the reflectances of G16 and G17 by 5%, which generally leads to an AOD difference of less than 0.05.

Note that it is difficult to compare the two ABI sensors directly. Such a comparison cannot be done by simply looking at the same scene at the same time, because the surface reflectance, as well as the atmospheric path, are different, which will introduce differences in ABI radiances. Instead, the comparison between the two ABI sensors will require selecting deep convective cloud scenes and performing statistical comparisons for those pixels, which is beyond the scope of the manuscript.

Appendix C2: SSA Uncertainty

We tested two extremes of assumed SSA (0.9 and 1.0) as inputs for creating lookup tables and checked the AOD that would be retrieved for those SSAs using the phase function determined by the AERONET inversion. As shown in Figure C2a, the results for SSA = 1 are similar to our base case of SSA = 0.968. While adjusting the single scattering albedo can force agreement with AERONET AOD for part of the timeline, the systematic difference between the two sensors after 22:00 UTC is still evident. This difference can only be corrected by adjusting the phase function over the appropriate angles. This observation emphasizes the value of dual-view geostationary observations.

Next, we repeated our procedure for the adjustment of the phase function. For the case of SSA = 0.9, there are larger differences over most of the period and poor agreement between the two retrievals after 22:00 UTC. Based on these AOD biases, adjustments to the initial phase function were performed assuming SSA = 0.9, and the resulting phase function is shown in Figure C2b, along with the adjusted phase function based on an assumed SSA = 0.968. As expected, the case of SSA = 0.9 leads to larger adjustments in phase function, but the adjustments in both cases are successful in attaining AOD agreement within 10% in Figure C2c.

The results show that it is possible to find a different combination of SSA and phase function that can match the observations and that aligns the retrievals from the two sensors. This finding points to the importance of an independent constraint on SSA. It may be possible to leverage more of the information in the geostationary data to assist with constraining SSA, but that should be explored in follow-on work.

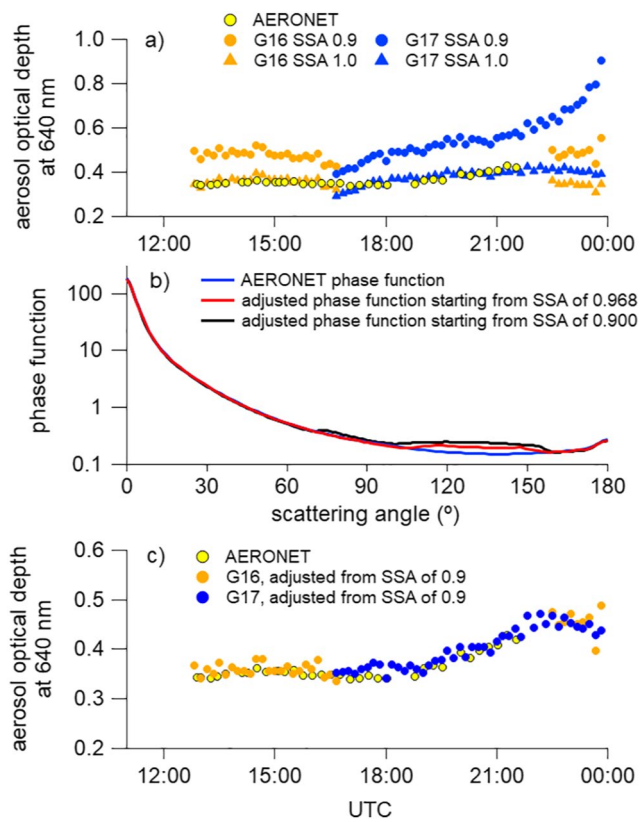

Figure C2. (a) Aerosol optical depth (AOD) retrievals at 640 nm for the Merida case study on June 24, 2019, using the Aerosol Robotic Network (AERONET) phase function but two different values for , single scattering albedo (SSA) (0.9 and 1.0). (b) Phase functions from the AERONET operational product (blue), the adjustments based on an assumed SSA of 0.968 (red), and the adjustments based on a given SSA of 0.9 (black). (c) The corresponding AOD retrievals at 640 nm using the phase function that has been adjusted assuming SSA = 0.9.

Appendix C3: Ocean Reflectance Uncertainty

The uncertainty in ocean surface reflectance is estimated by considering the chlorophyll-a concentration of 1.85 mg m^{-3} retrieved at the pixel of interest on June 24, 2019. Compared to the case with no chlorophyll-a, the increased concentration enhances the Lambertian component of the ocean reflectance. When used with the AERONET phase function, the increased ocean reflectance leads to lower AOD retrievals by 4% for G16% and 3% for G17 (Figure C3a). This reduces some of the high bias in Figure 5, but adjustments to the phase function are still necessary to achieve AOD agreement within 10%, as shown in Figures C3b and C3c.

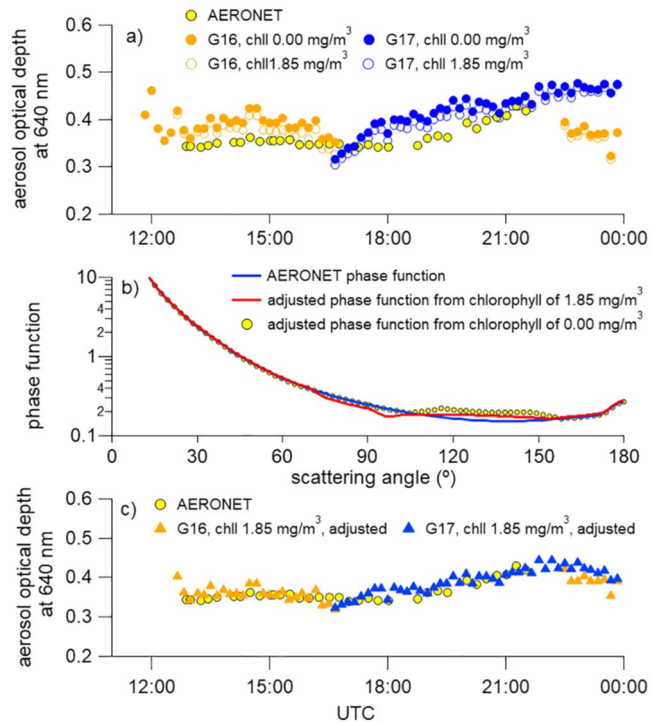

Figure C3. (a) G16 and G17 aerosol optical depth (AOD) retrievals for the Merida case study on June 24, 2019, using the Aerosol Robotic Network (AERONET) phase function and surface reflectances assuming chlorophyll-a concentrations of 0 mg m^{-3} and 1.85 mg m^{-3}. AODs from AERONET products are also shown. (b) The adjusted phase function, applying the methodology using the surface reflectances from different chlorophyll-a concentrations. (c) Same as (a), but using the adjusted phase function in (b).

Appendix D: Retrievals for the Remaining 18 Pixels

Retrievals for the remaining 18 pixels in Figure 10 are shown in Figure D1. Similar to the example given in Figure 11, the AOD differences between G16 and G17 operational retrievals in the overlap period are generally larger than those between G16 and G17 retrievals using the adjusted phase function. This evaluation indicates that the improved agreement between the G16 and G17AODs is robust.

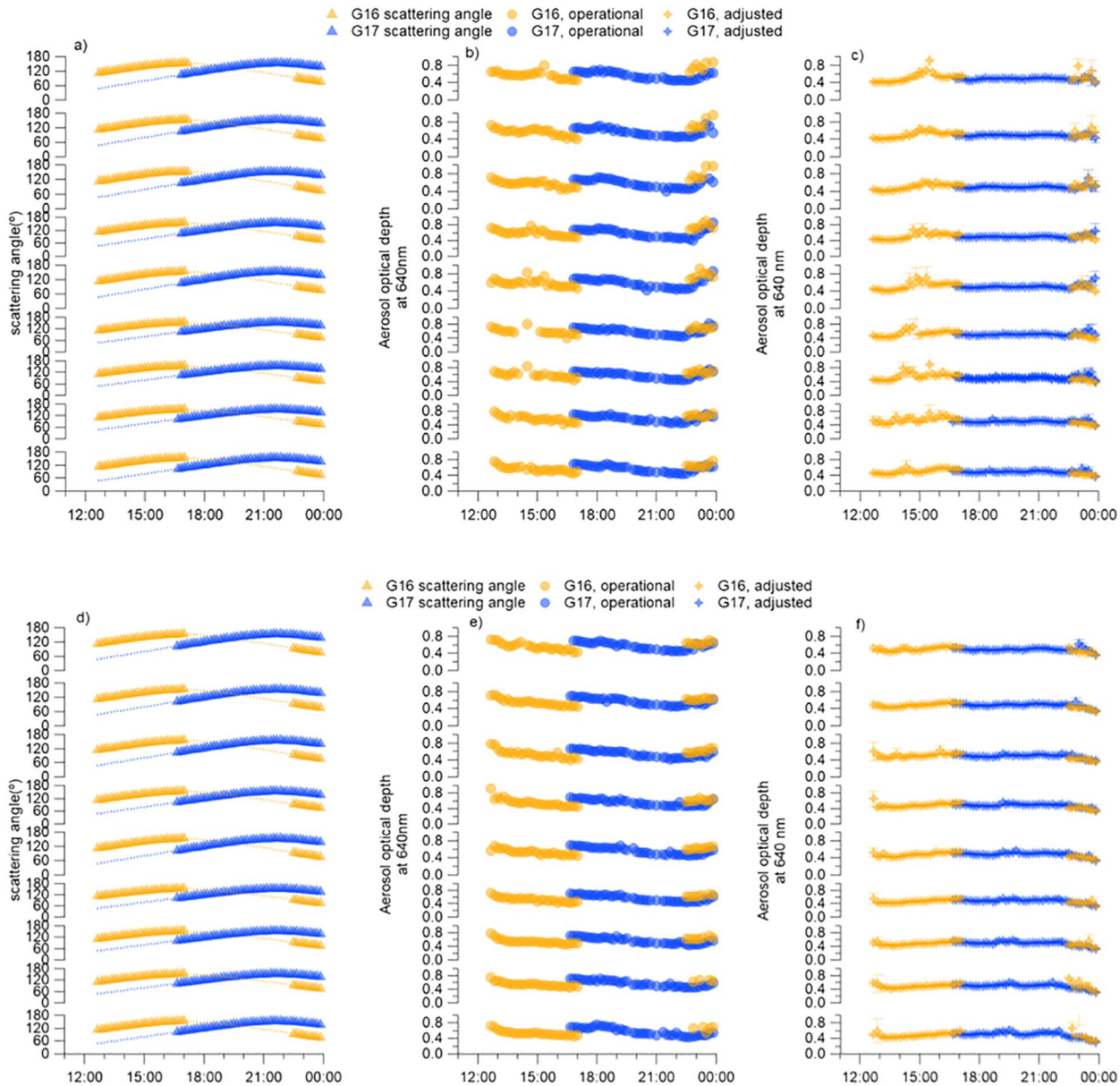

Figure D1. Plots of (a) scattering angles, and retrieved aerosol optical depths from (b) geostationary operational environmental satellites (GOES) operational products, and from (c) GOES observations but using the adjusted phase function, for the first 10 pixels in Figure 10 (ordered top to bottom, with the sixth pixel excluded). (d)–(f) are the same as (a)–(c), but for the last 10 pixels in Figure 10 (with the 12h pixel excluded).

Data Availability Statement

All the retrievals presented in the paper will be made freely available through the Mountain Scholar data repository. AERONET data and products can be freely accessed via https://aeronet.gsfc.nasa.gov/new_web/. The operational GOES aerosol products for both satellites were available as of January 1, 2019, at https://www.avl.class.noaa.gov/saa/products/search?sub_id=0&datatype_family=GRABIPRD&submit.x=28&submit.y=2.

Acknowledgments
This work is based upon research supported by the U. S. Office of Naval Research under Multidisciplinary University Research Initiative (MURI) Grant N00014-16-1-2040. J. Wang and X. Xu are supported by the same MURI grant to the University of Iowa. R. Kahn and J. A. Limbacher are supported by NASA's Climate and Radiation Research and Analysis Program under Hal Maring, the Atmospheric Composition Program under Richard Eckman, and the EOS Terra and MISR projects. NASA's Making Earth System Data Records for Use in Research Environments (MEaSUREs) program (NNH17ZDA001N-MEASURES) provided partial support of L. A. Remer and R. Levy. The authors thank Natalie Tourville and Matthew Rogers from Cooperative Institute for Research in the Atmosphere, and Shobha Kondragunta and Istvan Laszlo from NOAA/NESDIS Center for Satellite Applications and Research, for assistance with the ABI data and retrieval details. The authors thank Hector R. Estevez, Instituto de Geofísica, Universidad Nacional Autónoma de México, for his effort in establishing and maintaining the Mérida site. The authors thank our three anonymous reviewers whose insightful comments helped us to significantly improve the manuscript.

References

ABI AOD ATBD (2018). GOES-R Advanced Baseline Imager (ABI) algorithm theoretical basis document for suspended matter/aerosol optical depth and aerosol size parameter. NOAA/NESDIS/STAR. Version 4.2, 14 February 2018. Retrieved from https://www.star.nesdis.noaa.gov/smcd/spb/aq/AerosolWatch/docs/GOES-R_ABI_AOD_ATBD_V4.2_20180214.pdf

Bevan, S. L., North, P. R. J., Los, S. O., & Grey, W. M. F. (2012). A global dataset of atmospheric aerosol optical depth and surface reflectance from AATSR. *Remote Sensing of Environment*, *116*, 119–210. https://doi.org/10.1016/j.rse.2011.05.024

Carlson, T. N., & Prospero, J. M. (1972). The large-scale movement of Saharan air outbreaks over the Northern Equatorial Atlantic. *Journal of Applied Meteorology*, *11*, 283–297. https://doi.org/10.1175/1520-0450(1972)011<0283:tlsmos>2.0.co;2

Chýlek, P., Henderson, B. G., & Mishchenko, M. (2003). Aerosol radiative forcing and the accuracy of satellite aerosol optical depth retrieval. *Journal of Geophysical Research*, *108*(D24), 4764. https://doi.org/10.1029/2003JD004044

Cox, C., & Munk, W. H. (1954). The measurement of the roughness of the sea surface from photographs of the sun glitter. *Journal of the Optical Society of America*, *44*, 838–850. https://doi.org/10.1364/josa.44.000838

Diner, D. J., Beckert, J. C., Reilly, T. H., Bruegge, C. J., Conel, J. E., Kahn, R. A., et al. (1998). Multiangle image spectroradiometer (MISR) instrument description and experiment overview. *IEEE Transactions on Geosciences and Remote Sensing*, *36*, 1072–1087. https://doi.org/10.1109/36.700992

Ding, S., Wang, J., & Xu, X. (2016). Polarimetric remote sensing in O_2 A and B bands: Sensitivity study and information content analysis for vertical profile of aerosols. *Atmospheric Measurement Techniques*, *9*, 2077–2092. https://doi.org/10.5194/amt-9-2077-2016

Dubovik, O., Sinyuk, A., Lapyonok, T., Holben, B. N., Mishchenko, M., Yang, P., et al. (2006). Application of spheroid models to account for aerosol particle nonsphericity in remote sensing of desert dust. *Journal of Geophysical Research*, *111*, D11208. https://doi.org/10.1029/2005JD006619

Evans, K. F. (1998). The spherical harmonics discrete ordinate method for three-dimensional atmospheric radiative transfer. *Journal of the Atmospheric Sciences*, *55*, 429–446. https://doi.org/10.1175/1520-0469(1998)055<0429:Tshdom>2.0.Co;2

Francis, D., Fonseca, R., Nelli, N., Cuesta, J., Weston, M., Evan, A., & Temimi, M. (2020). The atmospheric drivers of the major Saharan dust storm in June 2020. *Geophysical Research Letters*, *47*, e2020GL090102. https://doi.org/10.1029/2020gl090102

Giles, D. M., Sinyuk, A., Sorokin, M. G., Schafer, J. S., Smirnov, A., Slutsker, I., et al. (2019). Advancements in the Aerosol Robotic Network (AERONET) Version 3 database – Automated near-real-time quality control algorithm with improved cloud screening for Sun photometer aerosol optical depth (AOD) measurements. *Atmospheric Measurement Techniques*, *12*, 169–209. https://doi.org/10.5194/amt-12-169-2019

Holben, B. N., Eck, T. F., Slutsker, I., Tanré, D., Buis, J. P., Setzer, A., et al. (1998). AERONET – Federated instrument network and data archive for aerosol characterization. *Remote Sensing of Environment*, *66*, 1–16. https://doi.org/10.1016/S0034-4257(98)00031-5

Hou, W., Wang, J., Xu, X., Reid, J., Janz, S., & Leitch, J. (2020). An algorithm for hyperspectral remote sensing of aerosols: 3. Application to the GEO-TASO data in KORUS-AQ field campaign. *Journal of Quantitative Spectroscopy & Radiative Transfer*, *253*, 22. https://doi.org/10.1016/j.jqsrt.2020.107161

Kahn, R., West, R., McDonald, D., Rheingans, B., & Mishchenko, M. I. (1997). Sensitivity of multiangle remote sensing observations to aerosol sphericity. *Journal of Geophysical Research: Atmospheres*, *102*(D14), 16861–16870. https://doi.org/10.1029/96jd01934

Kahn, R. A., & Gaitley, B. J. (2015). An analysis of global aerosol type as retrieved by MISR. *Journal of Geophysical Research: Atmospheres*, *120*, 4248–4281. https://doi.org/10.1002/2015JD02332210.1002/2015jd023322

Knapp, K. R., FrouinKondragunta, R. S., Prados, A., & Prados, A. (2005). Toward aerosol optical depth retrievals over land from GOES visible radiances: Determining surface reflectance. *International Journal of Remote Sensing*, *26*(18), 4097–4116. https://doi.org/10.1080/01431160500099329

Kolmonen, P., Sundström, A.-M., Sogacheva, L., Rodriguez, E., Virtanen, T. H., & de Leeuw, G. (2013). Uncertainty characterization of AOD for the AATSR dual and single view retrieval algorithms. *Atmospheric Measurement Techniques Discussions*, *6*, 4039–4075. https://doi.org/10.5194/amtd-6-4039-2013

Letu, H., Nagao, T. M., Nakajima, T. Y., Riedi, J., Ishimoto, H., Baran, A. J., et al. (2019). Ice cloud properties from Himawari-8/AHI next-generation geostationary satellite: Capability of the AHI to monitor the DC cloud generation process. *IEEE Transactions on Geoscience and Remote Sensing*, *57*, 3229–3239. https://doi.org/10.1109/tgrs.2018.2882803

Levy, R. C., Remer, L. A., & Dubovik, O. (2007). Global aerosol optical properties and application to moderate resolution imaging spectroradiometer aerosol retrieval over land. *Journal of Geophysical Research*, *112*, D13210. https://doi.org/10.1029/2006jd007815

Li, J., Carlson, B. E., & Lacis, A. A. (2015). Using single-scattering albedo spectral curvature to characterize East Asian aerosol mixtures. *Journal of Geophysical Research: Atmospheres*, *120*, 2037–2052. https://doi.org/10.1002/2014JD022433

Limbacher, J. A., & Kahn, R. A. (2019). Updated MISR dark water research aerosol retrieval algorithm – Part 2: Aerosol and surface-reflectance retrievals over shallow, turbid, and eutrophic water. *Atmospheric Measurement Techniques.*, *12*, 675–689. https://doi.org/10.5194/amt-12-675-2019

Lyapustin, A., Wang, Y., Korkin, S., & Huang, D. (2018). MODIS collection 6 MAIAC algorithm. *Atmospheric Measurement Techniques.*, *11*, 5741–5765. https://doi.org/10.5194/amt-11-5741-2018

Magzamen, S., Gan, R. W., Liu, J., O'Dell, K., Ford, B., Berg, K., et al. (2021). Differential cardiopulmonary health impacts of local and long-range transport of wildfire smoke. *GeoHealth*, *5*, e2020GH000330. https://doi.org/10.1029/2020GH000330

Mecikalski, J. R., Rosenfeld, D., & Manzato, A. (2016). Evaluation of geostationary satellite observations and the development of a 1–2 h prediction model for future storm intensity. *Journal of Geophysical Research: Atmospheres*, *121*, 6374–6392. https://doi.org/10.1002/2016JD024768

Miller, S. D. (2003). A consolidated technique for enhancing desert dust storms with MODIS. *Geophysical Research Letters*, *30*(20), 2071. https://doi.org/10.1029/2003GL018279

Nichols, N. T. A. (2020). *Saharan dust and pediatric asthma: A multinational, multiyear assessment in the Caribbean* (Doctoral dissertation). The University of Texas. Retrieved from https://hdl.handle.net/10735.1/9137

Prospero, J. M., & Lamb, P. J. (2003). African droughts and dust transport to the Caribbean: Climate change implications. *Science*, *302*, 1024–1027. https://doi.org/10.1126/science.1089915

Remer, L. A., Kaufman, Y. J., Tanré, D., Mattoo, S., Chu, D. A., Martins, J. V., et al. (2005). The MODIS aerosol algorithm, products, and validation. *Journal of the Atmospheric Sciences*, *62*(4), 947–973. https://doi.org/10.1175/jas3385.1

Remer, L. A., Tanré, D., Kaufman, Y. J., Levy, R. C., & Mattoo, S. (2006). Algorithm for remote sensing of tropospheric aerosol from MODIS: Collection 5. Product ID MOD04/MYD04.

Rothman, L. S., Gordon, I. E., Babikov, Y., Barbe, A., Chris Benner, D., Bernath, P. F., et al. (2013). The HITRAN 2012 molecular spectroscopic database. *Journal of Quantitative Spectroscopy and Radiative Transfer*, *130*, 4–50.

Saito, M., Yang, P., Ding, J., & Liu, X. (2021). A comprehensive database of the optical properties of irregular aerosol particles for radiative transfer simulations. *Journal of the Atmospheric Sciences*. https://doi.org/10.1175/JAS-D-20-0338.1

Sayer, A. M., Thomas, G. E., Grainger, R. G., Carboni, E., Poulsen, C., & Siddans, R. (2012). Use of MODIS-derived surface reflectance data in the ORAC-AATSR aerosol retrieval algorithm: Impact of differences between sensor spectral response functions. *Remote Sensing of Environment*, *116*, 177–188. https://doi.org/10.1016/j.rse.2011.02.029

Schmit, T. J., Griffith, P., Gunshor, M. M., Daniels, J. M., Goodman, S. J., & Lebair, W. J. (2017). A closer look at the ABI on the GOES-R series. *Bulletins of the American Meteorological Society*, *98*, 681–698. https://doi.org/10.1175/bams-d-15-00230.1

Shi, Y. R., Levy, R. C., Eck, T. F., Fisher, B., Mattoo, S., Remer, L. A., et al. (2019). Characterizing the 2015 Indonesia fire event using modified MODIS aerosol retrievals. *Atmospheric Chemistry and Physics*, *19*, 259–274. https://doi.org/10.5194/acp-19-259-2019

Si, Y., Lu, Q., Zhang, X., Hu, X., Wang, F., Li, L., & Gu, S. (2021). A review of advances in the retrieval of aerosol properties by remote sensing multi-angle technology. *Atmospheric Environment*, *244*(1), 117928. https://doi.org/10.1016/j.atmosenv.2020.117928

Sorensen, C., House, J. A., O'Dell, K., Brey, S. J., Ford, B., Pierce, J. R., et al. (2021). Associations between wildfire-related PM2.5 and Intensive Care Unit Admissions in the United States, 2006–2015. *GeoHealth*, *5*, e2021GH000385. https://doi.org/10.1029/2021GH000385

Spurr, R. (2006). VLIDORT: A linearized pseudo-spherical vector discrete ordinate radiative transfer code for forward model and retrieval studies in multilayer multiple scattering media. *Journal of Quantitative Spectroscopy & Radiative Transfer*, *102*, 316-342. https://doi.org/10.1016/j.jqsrt.2006.05.005

Tanré, D., Kaufman, Y. J., Herman, M., & Mattoo, S. (1997). Remote sensing of aerosol properties over oceans using the MODIS/EOS spectral radiances. *Journal of Geophysical Research*, *102*(D14), 16971–16988. https://doi.org/10.1029/96jd03437

Thomas, G. E., Carboni, E., Sayer, A. M., Poulsen, C. A., Sid- dans, R., & Grainger, R. G. (2009). In A. A. Kokhanovsky & G. de Leeuw (Eds.), *Oxford-RAL aerosol and cloud (ORAC): Aerosol retrievals from satellite radiometers in satellite aerosol remote sensing over land*. Springer.

Veefkind, J. P., de Leeuw, G., & Durkee, P. A. (1998). Retrieval of aerosol optical depth over land using two-angle view satellite radiometry during TARFOX. *Geophysical Research Letters*, *25*, 3135–3138. https://doi.org/10.1029/98gl02264

Vermote, E. F., Slonaker, R., Vibert, S., & Petrenko (2006). National Polar-orbiting Operational Environmental Satellite System (NPOESS) VIIRS Aerosol optical thickness and particle size parameter algorithm theoretical basis document, Version 5, Revision 8 June 2006, Document #: Y2388.

Wang, J., Christopher, S. A., Reid, J. S., Maring, H., Savoie, D., Holben, B. H., et al. (2003). GOES-8 retrieval of dust aerosol optical thickness over the Atlantic Ocean during PRIDE. *Journal of Geophysical Research*, *108*, 8595. https://doi.org/10.1029/2002JD002494

Wang, J., Liu, X., Christopher, S. A., Reid, J. S., Reid, E. A., & Maring, H. (2003). The effects of non-sphericity on geostationary satellite retrievals of dust aerosols. *Geophysical Research Letters*, *30*, 2293. https://doi.org/10.1029/2003GL018697

Wang, J., Xu, X., Ding, S., Zeng, J., Spurr, R., Liu, X., et al. (2014). A numerical testbed for remote sensing of aerosols, and its demonstration for evaluating retrieval synergy from a geostationary satellite constellation of GEO-CAPE and GOES-R. *Journal of Quantitative Spectroscopy & Radiative Transfer*, *146*, 510–528. https://doi.org/10.1016/j.jqsrt.2014.03.020

Wang, Y., Chen, L., Xin, J., & Wang, X. (2020). Impact of the dust aerosol model on the VIIRS aerosol optical depth (AOD) product across China. *Remote Sensing*, *12*, 991. https://doi.org/10.3390/rs12060991

Westphal, D. L., Curtis, C. A., Liu, M., & Walker, A. L. (2009). Operational aerosol and dust storm forecasting. *IOP Conference Series: Earth and Environmental Science*, *7*, 012007. https://doi.org/10.1088/1755-1307/7/1/012007

Xu, X., & Wang, J. (2015). Retrieval of aerosol microphysical properties from AERONET photo-polarimetric measurements: 1. Information content analysis. *Journal of Geophysical Research*, *120*, 7059–7078. https://doi.org/10.1002/2015JD023108

Xu, X., & Wang, J. (2019). UNL-VRTM, a testbed for aerosol remote sensing: Model developments and applications. In A. Kokhanovsky (Ed.), *Springer series in light scattering* (Vol. 4, pp. 1–69): Springer. https://doi.org/10.1007/978-3-030-20587-4_1

Xu, X., Wang, J., Wang, Y., Zeng, J., Torres, O., Yang, Y., et al. (2017). Passive remote sensing of altitude and optical depth of dust plumes using the oxygen A and B bands: First results from EPIC/DSCOVR at Lagrange-1 point, *Geophysical Research Letters*, *44*, 7544–7554. https://doi.org/10.1002/2017GL073939

Xu, X., Wang, J., Zeng, J., Spurr, R., Liu, X., Dubovik, O., et al. (2015). Retrieval of aerosol microphysical properties from AERONET photo-polarimetric measurements: 2. A new research algorithm and case demonstration. *Journal of Geophysical Research*, *120*, 7079–7098. https://doi.org/10.1002/2015JD023113

Yang, Y., Zhao, C., Sun, L., & Wei, J. (2019). Improved aerosol retrievals over complex regions using NPP visible infrared imaging radiometer suite observations. *Earth and Space Science*, *6*, 629–645. https://doi.org/10.1029/2019EA000574

Yu, F., Wu, X., Yoo, H., Wang, Z., Qian, H., & Shao, X. (2019). Radiometric calibration performance of GOES-17 advanced baseline imager (ABI). In *Earth observing Systems, XXIV, 111271C*. Retrieved from https://spie.org/Publications/Proceedings/Paper/10.1117/12.2531407?SSO=1

Zhang, H., Hoff, R. M., Kondragunta, S., Laszlo, I., & Lyapustin, A. (2013). Aerosol optical depth (AOD) retrieval using simultaneous GOES-East and GOES-West reflected radiances over the western United States. *Atmospheric Measurement Techniques*, *6*, 471–486. https://doi.org/10.5194/amt-6-471-2013

Zhang, H., Kondragunta, S., Laszlo, I., & Zhou, M. (2020). Improving GOES advanced baseline imager (ABI) aerosol optical depth (AOD) retrievals using an empirical bias correction algorithm. *Atmospheric Measurement Techniques*, *13*, 5955–5975. https://doi.org/10.5194/amt-13-5955-2020

Zhou, Y., Levy, R. C., Remer, L. A., Mattoo, S., Shi, Y., & Wang, C. (2020). Dust aerosol retrieval over the oceans with the MODIS/VIIRS Dark-Target algorithm: 1. Dust detection. *Earth and Space Science*, *7*, e2020EA001221. https://doi.org/10.1029/2020EA001221